Thermoelectric properties of single-phase n-type $Bi_{14}Te_{13}S_8$

Raphael Fortulan,[†,‖] Sima Aminorroaya Yamini,[*,‡] Azib Juri,[¶] Illia Serhiienko,[§,⊥] and Takao Mori[§,⊥]

†*Department of Computer Science and Creative Technologies, UWE, Bristol, UK*

‡*Centre for Microscopy and Microanalysis, University of Queensland, St. Lucia, Qld, 4072, Australia*

¶*Materials and Engineering Research Institute, Sheffield Hallam University, Sheffield S1 1WB, UK*

§*International Center for Materials Nanoarchitectonics (WPI-MANA), National Institute for Materials Science, Tsukuba 305-0044, Japan*

‖*Materials and Engineering Research Institute, Sheffield Hallam University, Sheffield S1 1WB, UK*

⊥*Graduate School of Pure and Applied Science, University of Tsukuba, Tsukuba 305-8577, Japan*

E-mail: s.aminorroaya@uq.edu.au

Abstract

Bismuth telluride (Bi_2Te_3) and its alloys are among the best thermoelectric materials at room temperature. $Bi_{14}Te_{13}S_8$, a material with a similar crystal structure, contains sulphur that can potentially improve thermoelectric performance through widening band gap and reduced lattice thermal conductivity. This compound forms in sulphur added Bi_2Te_3 alloys. Here, polycrystalline iodine-doped $Bi_{14}Te_{13}S_8$ sample is

investigated; an optimum iodine concentration of 1 at. % resulted in the power factor of 3.5 $mW^2\,m^{-1}\,K^{-1}$ at room temperature. Iodine doping reduced the lattice thermal conductivity for more than 30% by enhancing phonon scattering. An improved thermoelectric figure of merit zT of ∼0.29 at 520 K was obtained for 1-1.5 at% iodine doped $Bi_{14}Te_{13}S_8$. First-principles calculations indicate that $Bi_{14}Te_{13}S_8$ has a larger band gap compared to bismuth telluride, which allows for a reduction in the bipolar effect, however, a lower effective mass reduced the thermopower for a similar carrier concentration. This study demonstrates that tuned iodine doping can effectively optimise the thermoelectric performance of $Bi_{14}Te_{13}S_8$, highlighting its contribution in multiphase sulphur alloyed Bi_2Te_3-based materials.

Introduction

Thermoelectric Bi_2Te_3 and its alloys with sulphur have been the focus of extensive research;[1–6] we have shown the alloying of Bi_2Te_3 with Bi_2S_3 introduces a secondary phase of $Bi_{14}Te_{13}S_8$ in the matrix of Bi_2Te_3,[7] however, the thermoelectric properties of $Bi_{14}Te_{13}S_8$ have not been intensely studied.[8] Sulphur is a non-toxic and abundant, relative to tellurium and therefore, the thermoelectric properties of its compounds are of the interest of researchers.[9]

Previous works referred to $Bi_{14}Te_{13}S_8$ as Bi_2Te_2S and its electronic transport properties have been studied by several research groups.[10–13] $Bi_{14}Te_{13}S_8$ has a layered rhombohedral crystal structure similar to Bi_2Te_3, with alternating layers of Bi-Te and Bi-S bonds along the c-axis, allowing for lower values of thermal conductivity.[11] Researchers have also explored alloying the material with antimony, widely used in Bi_2Te_3-based materials,[14–16] to achieve even lower values of thermal conductivity while maintaining high carrier mobility.[17]

In this structure, some of Te atoms are replaced with lighter, more electronegative S atoms, widens the band gap compared to Bi_2Te_3, potentially allowing for a higher thermopower.

The wider band gap of $Bi_{14}Te_{13}S_8$ compared to Bi_2Te_3 allows for reduction of the bipolar effect which deteriorates the performance of this compound at temperatures higher than 400 K,[6,18,19] due to a reduction in thermopower. Several efforts have been made to suppress the effect of minority charges in Bi_2Te_3-based compounds by tuning the carrier concentration[20,21] and enlarging the band gap.[22–24] Record high values of zT have been achieved through alloying Bi_2Te_3 with Sb[25] and Se.[26,27] However, the necessity for higher performance for temperatures over 500 K still persists.[28]

Similar to Bi_2S_3-based compounds,[29,30] high resistivity values present an obstacle for achieving higher values of figure-of-merit for $Bi_{14}Te_{13}S_8$,[11,31] creating a need to study the effects of carrier concentration tuning in this material.

In this work, we synthesise polycrystalline iodine doped $Bi_{14}Te_{13}S_8$ samples to investigate the effect of iodine on the electronic transport properties of this compound. The optimum concentration of iodine is determined to maximise the power factor through controlled changes in carrier concentration while suppressing harmful minority carrier conduction.

Experimental details

Synthesis

A set of $Bi_2(Te_{1.857}S_{1.142})_{1-x}I_x$ (x = 0, 0.005, 0.01, 0.015, and 0.02) samples were synthesised by direct reaction of stoichiometric amounts of high purity Bi (99.999%, Alfa Aesar), Te (99.999%, Alfa Aesar) shots, dried S (99.99%, Alfa Aesar) powder, and BiI_3 (99.999%, Alfa Aesar Puratronic®) powder in vacuum sealed quartz tubes in an inert atmosphere glove box. The tubes were homogenised at 850 °C for 16 h, quenched in cold water, and annealed at 450 °C for 72 h. The obtained ingots were hand-ground into fine powders in an agate mortar and pestle inside an inert atmosphere glove box. The powders were then loaded

into a graphite die and sintered under vacuum to produce 11 mm diameter rods using spark plasma sintering (Dr. Sinter-1080 SPS system, Fuji-SPS, Japan) at 400 °C and an axial pressure of 50 MPa for 5 min. The relative density of the sintered samples, calculated from the weight and dimensions of the rods, was ≥99% for all the samples.

Materials characterisation

Phase purity and crystal structure of the sintered samples were characterised by X-ray diffraction (XRD) using a PANalytical X'Pert PRO X-ray diffractometer with Cu-Kα1 radiation ($\lambda = 1.54059$ Å, 40 kV, 40 mA). Rietveld refinements were performed on the acquired diffraction patterns using the GSAS-II software.[32]

The electronic transport properties of the sintered samples were investigated in the parallel direction to the sintering pressure by cutting $\sim 2 \times 2 \times 8$ mm^3 bars from the sintered rods, parallel to the sintering direction. The measurements were carried out from room temperature to 520 K under a helium atmosphere using a Linseis LSR-3 apparatus.

The thermal transport properties of the samples were investigated parallel to the sintering pressure by cutting out a disc with a diameter and thickness of approximately 10 mm and 1.5 mm, respectively, from the sintered rods. The thermal conductivities (κ) were calculated using the thermal diffusivity (D), specific heat capacity (c_p), and density (d) of the samples, $\kappa = D \cdot c_p \cdot d$. The thermal diffusivity was measured using a Netzsch LFA-467 Hyperflash® instrument. The specific heat capacity was measured using a PerkinElmer-DSC 8000 differential scanning calorimeter in compliance with the sapphire standard ASTM E1269-11(2018) test.[33]

The disc-shaped samples were also used to measure carrier concentration and electronic mobility using the van der Pauw technique with an ECOPIA HMS 3000 Hall measurement

system.

Electronic structure calculation

DFT calculations were employed to qualitatively study the electronic band structure of the pristine sample. The PBE and GGA exchange-correlation functionals were used.[34] Monkhorst-Pack procedure was used to generate $10 \times 10 \times 10$ k-points for the Brillouin zone.[35] The plane wave/pseudopotential approach was employed, with a kinetic energy cut-off of 45 Ry for the wavefunctions and 360 Ry for the electron density. The crystal structure used was that of the Rietveld refined pristine sample.

Results and discussion

Structural and phase analysis

Figure 1 shows the XRD patterns of all samples analysed. The diffraction patterns confirm the existence of a single rhombohedral phase of $Bi_{14}Te_{13}S_8$ crystal belonging to the space group $R\bar{3}$ (PDF Card - 04-009-4602). The enlarged view of the main diffraction peak is shown in the inset, where it can be seen that the peak slight shifted with the dopant addition.

The lattice parameters for each sample were determined using Rietveld refinement of the XRD patterns (Table 1). As shown in Figure 2, the lattice parameters exhibit variation with the presence of the dopant, where a = b parameters show an overall decline, while the c parameter fluctuates with the dopant concentration. These changes in the lattice parameters can be attributed to the differences in ionic radii of S^{2-} (0.184 nm), Te^{2-} (0.221 nm), and I^{1-} (0.22 nm).[36] Similar behaviour was observed in iodine-doped Bi_2Te_3, albeit to a lesser extent due to the relatively similar radii of Te^{2-} and I^{1-}.[37,38] Nevertheless, the obtained values are consistent with literature-reported values of a = b = 1.1269 nm and c = 1.1129 nm.[39]
It is worth noting that all samples exhibited a preferred orientation in the {006} lattice plane,

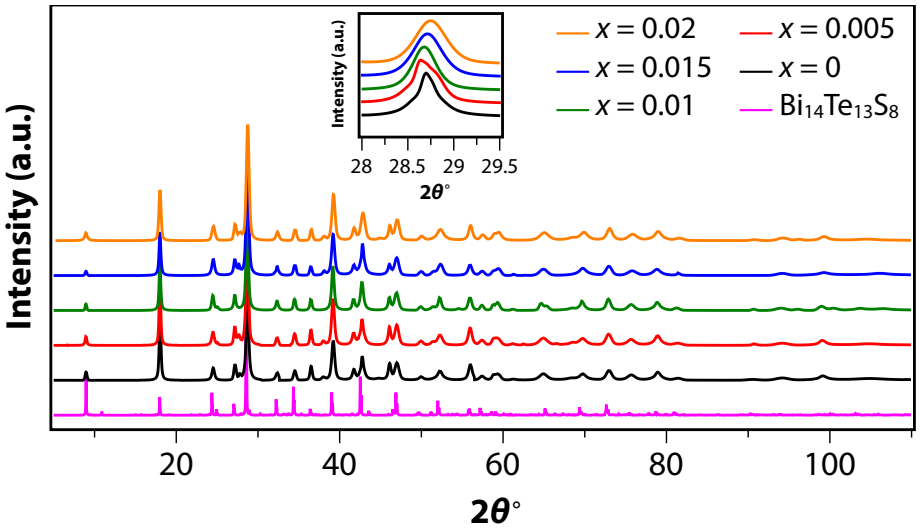

Figure 1: X-ray diffraction patterns of $Bi_2(Te_{1.857}S_{1.142})_{1-x}I_x$ (x = 0, 0.005, 0.01, 0.015, and 0.02) in the range of 5° to 108°. The inset shows the enlarged view of the main diffraction peak.

Table 1: Refined lattice parameters of $Bi_2(Te_{1.857}S_{1.142})_{1-x}I_x$ (x = 0, 0.005, 0.01, 0.015, and 0.02)

x	a = b (Å)	c (Å)
0	11.2198	29.6539
0.005	11.2174	29.6318
0.01	11.2210	29.6279
0.015	11.2140	29.6473
0.02	11.2128	29.6494

as illustrated in Figure 3. This was also observed in samples of $Bi_2Te_{2-x}S_{1-x}$[8] and it is likely due to the preferred crystal growth in the basal plane parallel to the ingot growth direction[40] that might be enhanced by the sintering process.[41,42] Much like Bi_2Te_3, $Bi_{14}Te_{13}S_8$ exhibits three covalently bonded quintuple layers of $\left[Te^{(1)}/S^{(1)} - Bi - S^{(2)} - Bi - Te^{(1)}/S^{(1)}\right]$ sheets stacked along the c-axis.[43] These layers interact weakly through van der Waals interactions.[39] Here, the superscripts (1) and (2) were used to distinguish the two types of atomic bonding, where (1) denotes a weak van der Waals attraction and (2) denotes a covalent bonding. Note that this crystal structure has been erroneously referred to as "Bi_2Te_2S" in some works.[10,44] Pauling[39] realised that the "Bi_2Te_2S" crystal structure was unlikely to be stable at this

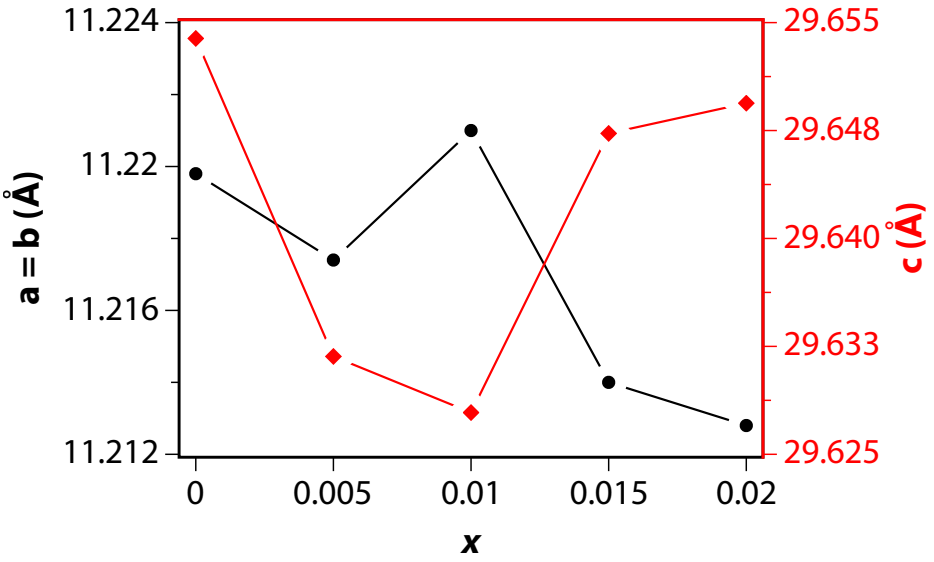

Figure 2: Variation of lattice parameters a = b and c with the dopant concentration x.

stoichiometry due to a substantial strain localised on the internal sulphur layer within the stacking sequence. This strain is due to the considerable difference in ionic radii between S and Te, which would result in a large size mismatch between the hexagonal, closely packed S and Te layers. To relieve this strain and stabilise the structure, formula of $Bi_{14}Te_{13}S_8$ was suggested in which S only occupies the $Te^{(1)}$ sites in the Bi_2Te_3 structure.[45]

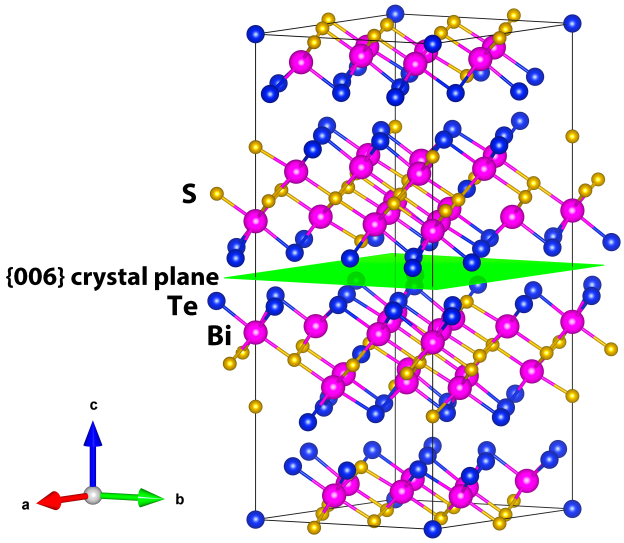

Figure 3: Crystal structure of $Bi_{14}Te_{13}S_8$ and {006} crystal plane.

Band structure analysis

The calculated electronic band structure of $Bi_{14}Te_{13}S_8$ using the refined lattice parameters for the original sample as described in Table 1 is shown in Figure 4. The band structure shows that this is a direct band gap semiconductor, with the conduction band minimum and the valence band maximum centred around the Γ point in reciprocal space.

The obtained band gap for $Bi_{14}Te_{13}S_8$ is about 0.14 eV. However, it is well known that traditional DFT calculations, such as PBE (used in this work), underestimate the value of the band gap[46–50] with the errors mainly due to: (1) self-interaction errors due to interactions of an electron with itself in the Coulomb repulsion term of the density functional;[49,51] and (2) the Kohn-Sham eigenvalues, which stem from using the differences of the ground state energies of the Kohn-Sham system as the band gap.[52,53]

The value calculated here is smaller than those presented in the Open Quantum Materials (∼0.5 eV),[54] JARVIS-DFT (∼0.36 eV),[55] and Materials Project (∼0.55 eV)[56] databases, and it also differs from previous works, of ∼0.34 eV[57] using PBE + spin-orbit coupling, and of ∼0.68 eV using hybrid functionals + spin-orbit coupling.[57] However, the overall trend points out that $Bi_{14}Te_{13}S_8$ is a narrow band semiconductor with a larger band gap compared to Bi_2Te_3, in agreement with the fact that the higher electronegativity of S (compared to Te) should reduce the valence band maximum of the material.[45] The increased band gap can help to reduce the contribution of the bipolar effect in this material,[58] potentially allowing higher values of zT at high temperatures.[59]

Figure 4: Band structure of $Bi_{14}Te_{13}S_8$.

Transport properties analysis and figure of merit zT

The temperature dependent thermopower and electrical resistivity of all samples are shown in Figures 5(a) and 5(b). All samples show a negative value for the thermopower, indicating n-type semiconductor behaviour. At room temperature, the values of the thermopower

vary between ∼-130 µV K^{-1} for the undoped sample to ∼-44 µV K^{-1} for the heavily doped sample with $x = 0.02$. The thermopower for the pristine sample showed an upward trend at higher temperatures, likely due to with the presence of the bipolar effect usually seen in narrow band gap semiconductors.[60–62,62] The enhanced carrier concentration of the doped samples suppressed the contribution of minority carriers and a linear relationship between temperature and thermopower was observed as described by Mott's rule.[63]

The electrical resistivity showed an inverse trend relative to the thermopower with the highest value of about 5.8 mΩ cm for the undoped sample and the lowest value of about 1.2 mΩ cm for the heavily doped sample with $x = 0.02$. All samples exhibited a metallic behaviour, with the electrical resistivity increasing with temperature. In particular, the thermopower and electrical resistivity showed similar values for the samples with $x = 0.005$, $x = 0.01$, and $x = 0.015$.

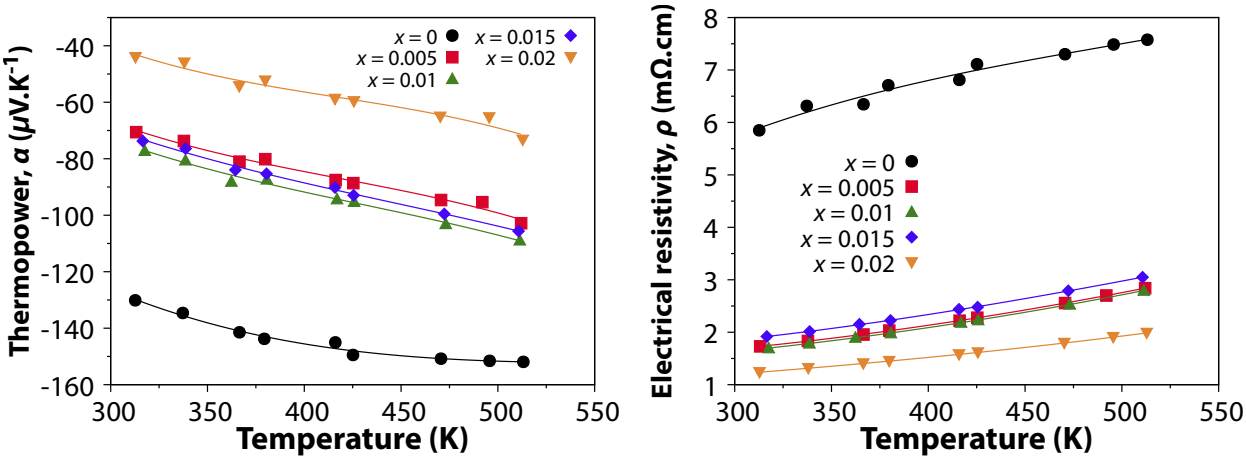

(a) (b)

Figure 5: Temperature dependence of the (a) thermopower and (b) electrical resistivity of $Bi_2(Te_{1.857}S_{1.142})_{1-x}I_x$ ($x = 0$, 0.005, 0.01, 0.015, and 0.02) from 300 and 520 K.

The choice of iodine as a dopant in Bi_2Te_3 is typically effective, leading to noticeable changes in electrical resistivity due to controlled variations in carrier concentration,[38,64–66] given to the similarity in radii of Te^{2-} and I^{1-}. However, in the case of Bi_2S_3 it was observed that iodine was not as successful as a dopant.[67]

In this set of samples, both Te and S are present, and both have been accounted for substitution with I. Assuming that the changes are caused by the incorporation of I at the sites of both Te and S, the carrier concentration would be governed by the following defect chemistry reaction the incorporation of I at the sites of both Te and S, the carrier concentration would be governed by the following defect chemistry defect reaction

$$\mathrm{Bi_{14}Te_{13-1.85\frac{x}{3}}S_{8-1.15\frac{x}{3}}I_x} \longrightarrow \left(1.85\frac{x}{3}\mathrm{I_{Te}^{\bullet}} + 1.85\frac{x}{3}\mathrm{e^{'}}\right) + \left(1.15\frac{x}{3}\mathrm{I_{S}^{\bullet}} + 1.15\frac{x}{3}\mathrm{e^{'}}\right). \qquad (1)$$

Equation 1 predicts that the incorporation of high concentrations, x, of iodine will increase the carrier concentration in $Bi_{14}Te_{13}S_8$. To test this hypothesis, room temperature Hall effect measurements were conducted on samples with varying iodine doping concentrations. The results, summarised in Table 2, reveal that while carrier mobility (μ_H) decreases monotonically with increasing iodine concentration from a maximum of $75.24\,cm^2\,V^{-1}\,s^{-1}$ at $x = 0$ to a minimum of $22.29\,cm^2\,V^{-1}\,s^{-1}$ at $x = 0.02$, the dependence of carrier concentration on iodine doping is more complex. Specifically, the carrier concentration remains relatively constant for $x = 0.005$, 0.01, and 0.015 before increasing significantly at $x = 0.02$.

Table 2: Room-temperature Hall carrier concentration (n_H) and Hall mobility (μ_H) of $Bi_2(Te_{1.857}S_{1.142})_{1-x}I_x$ ($x = 0$, 0.005, 0.01, 0.015, and 0.02)

x	n_H ($\times 10^{19}\,cm^{-3}$)	μ_H ($cm^2\,V^{-1}\,s^{-1}$)
0	−1.41	75.24
0.005	−5.3	68.50
0.01	−5.47	68.22
0.015	−5	64.68
0.02	−22.8	22.29

The trends in electrical resistivity (see Figure 5(b)) further illustrate the effect of doping on the carrier concentration. The resistivity ρ shows a significant decrease from its maximum value for the undoped sample, maintaining similar values of $\sim$1.7 mΩ cm for $0.05 \leq x \leq 0.015$ before dropping to its minimum at $x = 0.02$.

Similarly, given the inverse relationship between carrier concentration and thermopower α,

the undoped sample has the largest thermopower magnitude due to its lowest carrier concentration, whereas the $x = 0.02$ sample has the smallest thermopower magnitude corresponding to its highest carrier density. Since the samples with $x = 0.005$, 0.01, and 0.015 have comparable carrier concentrations, they have shown similar thermopower values of -80 $\sim$ -70 $\mu V\,K^{-1}$. Overall, the transport data confirm the existence of a critical iodine doping range between 0.015 ¡ x ¡ 0.02. A similiar behaviour was observed for iodine doped Bi_2S_3.[67]

At room temperature and with similar carrier concentrations, the thermopower value for Bi_2Te_3 ($\sim$-238 $\mu V\,K^{-1}$ at $n_H = 1\ 10^{19}\,cm^{-3}$ is larger than the one presented here, which indicates that this compound has a lower effective mass than Bi_2Te_3. However, thermopower value of Bi_2S_3 ($\sim$-320 $\mu V\,K^{-1}$ at lower carrier concentrations of $n_H = 0.45\ 10^{19}\,cm^{-3}$) suggests a similar effective mass for this sample and Bi_2S_3.

To understand the influence of the band structure on the thermopower, the single parabolic band model (SPB) was used to analyse the measured transport and carrier concentration data. The SPB model is described by the following set of equations

$$\alpha = \pm\frac{k_B}{e}\left(\frac{2F_1(\eta)}{F_0(\eta)} - \eta\right), \tag{2a}$$

$$n = \frac{(2m^* k_B T)^{3/2}}{2\pi^2\hbar^3} F_{1/2}(\eta), \tag{2b}$$

where e is the elementary charge, k_B is the Boltzmann constant, $\eta = \frac{E_F}{k_B T}$ is the reduced Fermi level, $\hbar$ is the reduced Planck constant, m^* is the density of states effective mass, and $F_j(\eta)$ is the Fermi-Dirac integral for an index j and is defined as

$$F_j(\eta) := \int_0^\infty \frac{\varepsilon^j}{\exp(\varepsilon - \eta) + 1} d\varepsilon, \tag{3}$$

where $\varepsilon = \frac{E}{k_B T}$ is the reduced energy.

The fitted density of states effective mass was found to be $m^* \approx 0.65m_0$, where m_0 is the electron rest mass. The measured thermopower and carrier concentrations follow the trend predicted by the SPB model, as shown in the Pisarenko plot in Figure 6. Understandably, the relatively low effective mass of $Bi_{14}Te_{13}S_8$ compared to Bi_2Te_3 ($m^* \approx 1.06m_0$ [68,69]) can explain the low thermopower values observed even at lower carrier concentrations as predicted by Mott's rule.

For comparison, data from pristine Bi_2Te_3 samples[5,6,68] and Bi_2S_3 samples,[6,29,70,71] and samples of similar composition to that used in this work of chlorine doped $Bi_2Te_{1.93}S_{1.07-y}Cl_y$ and $Bi_2Te_{1.83}S_{1.17}$[8] was added to the plot. As can be seen from the Pisarenko plot, $Bi_{14}Te_{13}S_8$ closely follows the band structure of both Bi_2S_3 and similar compositions of $Bi_2Te_{1.93}S_{1.07-y}Cl_y$ and $Bi_2Te_{1.83}S_{1.17}$.

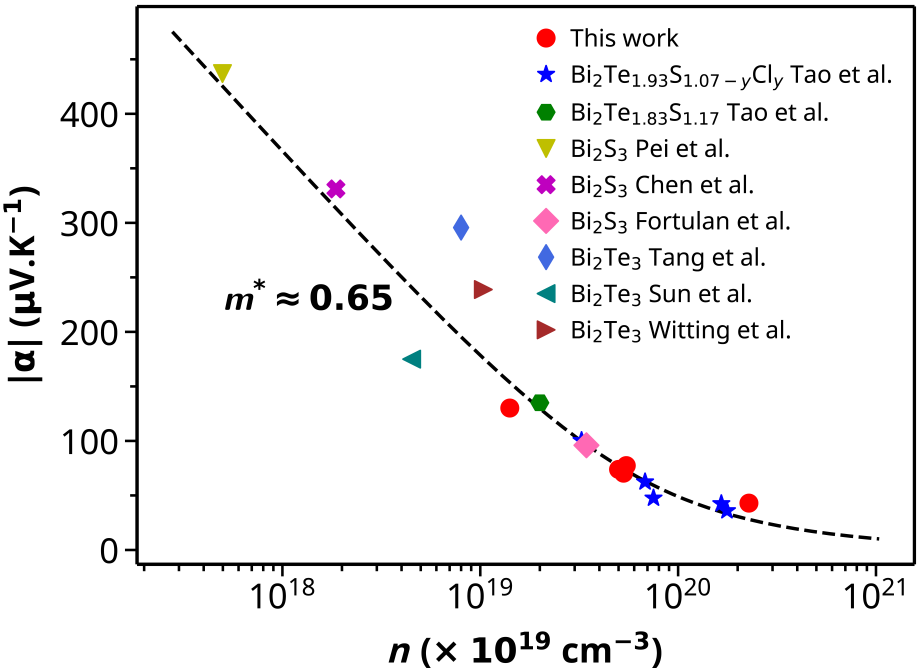

Figure 6: The Pisarenko plot (thermopower versus Hall carrier concentration) at room temperature of $Bi_2(Te_{1.857}S_{1.142})_{1-x}I_x$. The dashed line represents the calculated values from the SPB model using the fitted effective mass. Data from Bi_2Te_3,[5,6,68] Bi_2S_3,[6,29,70,71] $Bi_2Te_{1.93}S_{1.07-y}Cl_y$ and $Bi_2Te_{1.83}S_{1.17}$[8] are included for comparison.

Figure 7 shows the power factor (PF) values for all samples. Despite the reduced electrical resistivity, the reduced thermopower at higher doping concentrations resulted in similar,

modest power factor values of approximately 2.8 $\mathrm{mW\,m^{-2}\,K^{-1}}$ for the undoped, $x = 0.005$, and $x = 0.015$ samples. The heavily doped $x = 0.02$ sample exhibited the lowest power factor of $\sim$1.5 $\mathrm{mW\,m^{-2}\,K^{-1}}$, while $x = 0.01$ gave the optimum PF of $\sim$3.5 $\mathrm{mW\,m^{-2}\,K^{-1}}$.

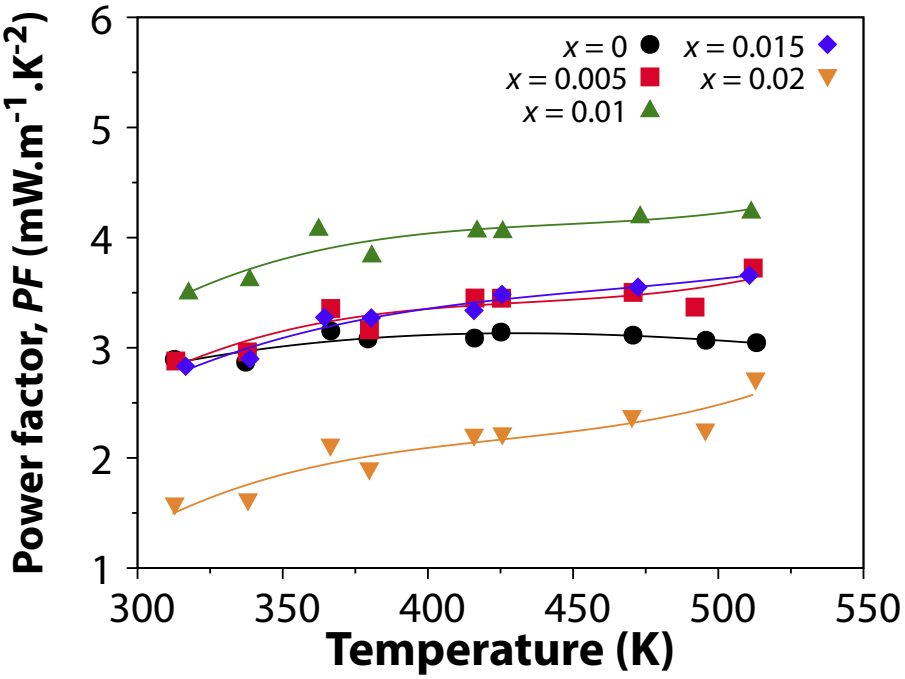

Figure 7: Temperature dependence of the power factor of $Bi_2(Te_{1.857}S_{1.142})_{1-x}I_x$ ($x = 0$, 0.005, 0.01, 0.015, and 0.02) from 300 and 520 K.

To understand the heat transport mechanisms existent in the material, high temperature measurements of the specific heat capacity of pristine $Bi_{14}Te_{13}S_8$ were conducted and are exhibited in Figure 8. At this temperature range of 300 $\sim$ 500 K, the specific heat capacity has values very close to those predicted by the Dulong-Petit law[72] with a linear trend (c_p = 0.16500(8) + 1.769(19) $\times$ $10^{-5}T$ $\mathrm{J\,g^{-1}\,K^{-1}}$). At this temperature range, the specific heat capacity can be fitted using the Debye model,[73] which leads to a Debye temperature of θ_D = 190.0(2.3) K and an average speed of sound of v = 2001(24) $\mathrm{m\,s^{-1}}$. It is worth noticing that due to the non-availability of lower temperature measurements to fit the specific heat capacity, these values can only be understood as approximations.

The thermal conductivity (κ) as a function of the temperature is shown Figure 9(a) and it increases with the presence of the dopant. The electronic contribution to thermal conductiv-

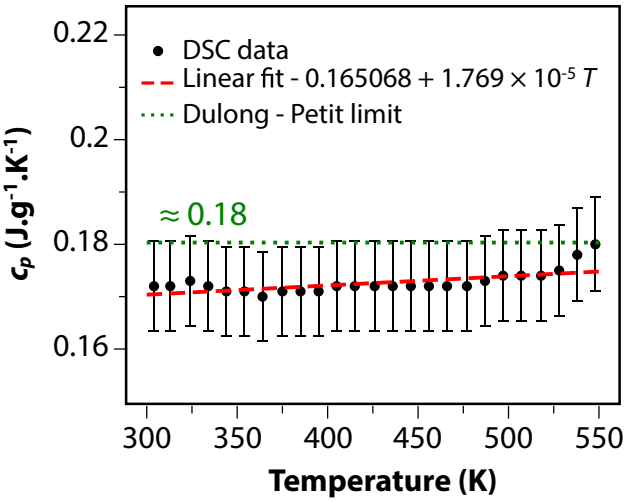

Figure 8: Temperature dependence of specific heat capacity of $Bi_{14}Te_{13}S_8$ from 300 to 550 K. The dotted green line represents the Dulong-Petit limit for the material and the dashed red line represents a linear fit of the data.

ity, i.e., the electronic thermal conductivity κ_e, was determined from the Wiedemann-Franz law[63] and shown in Figure 9(b). The Lorenz number was evaluated using the SPB model as follows

$$L = \left(\frac{k_B}{e}\right)^2 \frac{3F_0(\eta)F_2(\eta) - 4F_1(\eta)^2}{F_0(\eta)^2}. \quad (4)$$

As expected, with the increase in electrical conductivity with the dopant addition, the electronic thermal conductivity also increased for the doped samples. The lattice thermal conductivity was estimated from $\kappa_l = \kappa - \kappa_e$ and plotted in Figure 9(c). With the presence of the dopant, the lattice thermal conductivity was reduced and has already been seen in literature.[74–78] The heavily doped sample showed higher values than the moderately doped $x = 0.015$ (as seen e.g. in[67,79]) and this may be due to clustering of the dopant atoms leading to a decrease in scattering centres for phonons and an increase in lattice thermal conductivity. At room temperature, the maximum value of κ_l was observed for the undoped sample with $\sim$ 0.69 W m^{-1} K^{-1} and a minimum of $\sim$0.47 W m^{-1} K^{-1} for the sample with $x = 0.015$ (Figure 9(c)). The values exhibited by this material are in the lower range of the ones observed for telluride compounds,[80] as can be seen in the violin plot shown in Figure 9(d).

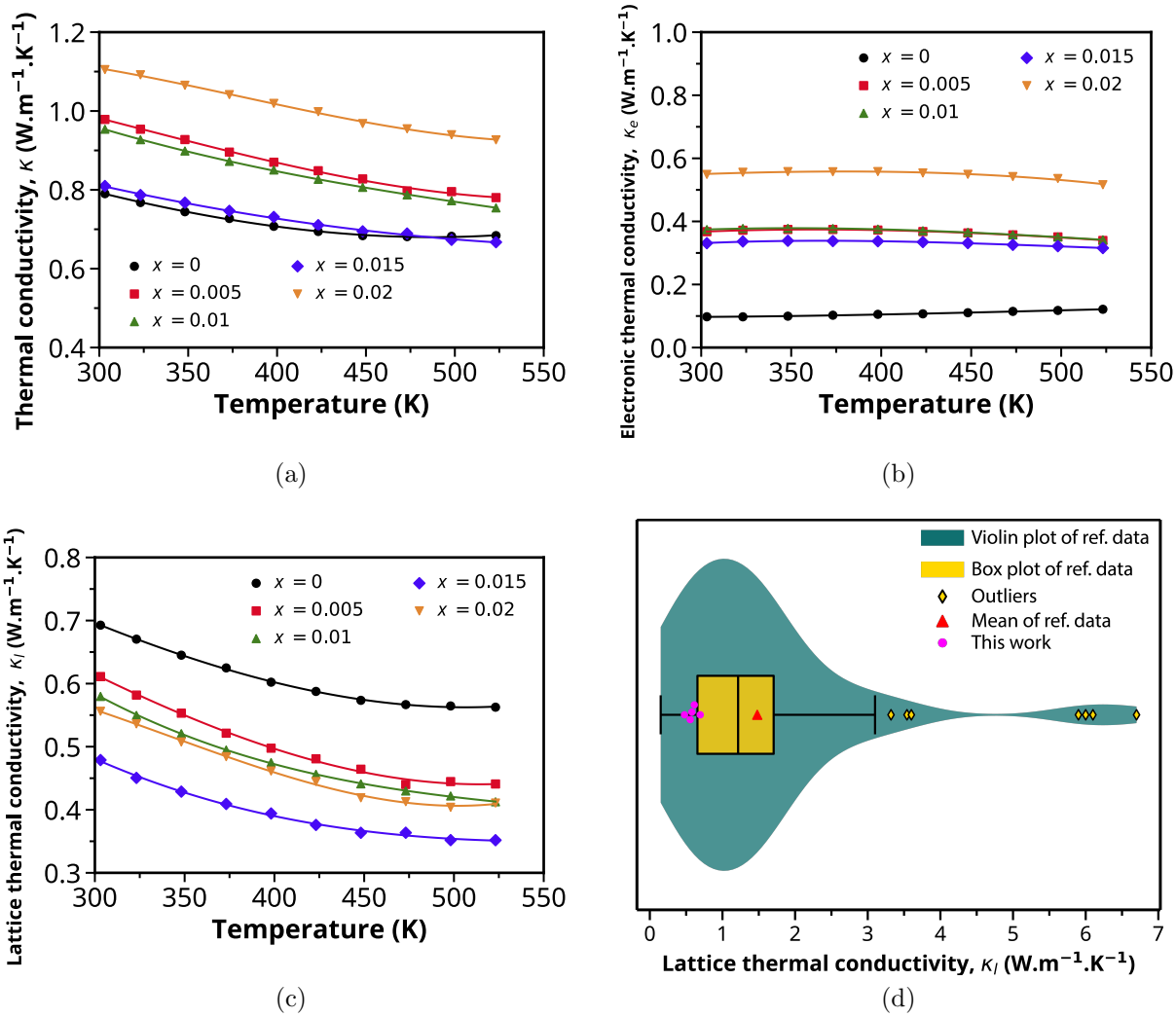

Figure 9: Temperature dependence of the (a) thermal conductivity, (b) electronic thermal conductivity, and (c) lattice thermal conductivity of $Bi_2(Te_{1.857}S_{1.142})_{1-x}I_x$ ($x = 0$, 0.005, 0.01, 0.015, and 0.02) between 300 to 520 K; (d) violin plot of lattice thermal conductivity data of literature data[80] compared with this work, all values are at room temperature.

Figure of merit zT

The figure of merit, zT, for the samples can be observed in Figure 10. The samples with $x =$ 0.01 and 0.015 achieved a maximum value zT of ~0.289 at 520 K. The presence of dopants resulted in a shift to the higher value of zT towards higher temperatures. The increase in the figure of merit was mainly due to the optimised power factor and a sharp reduction in the lattice thermal conductivity compared to the undoped sample. The values of zT observed

here are higher than the ones seem for pristine Bi_2Te_3[5] and Bi_2S_3[29] but lower than ones observed for sulphur-alloyed Bi_2Te_3[8,81] as can be seen in Figure **??**.

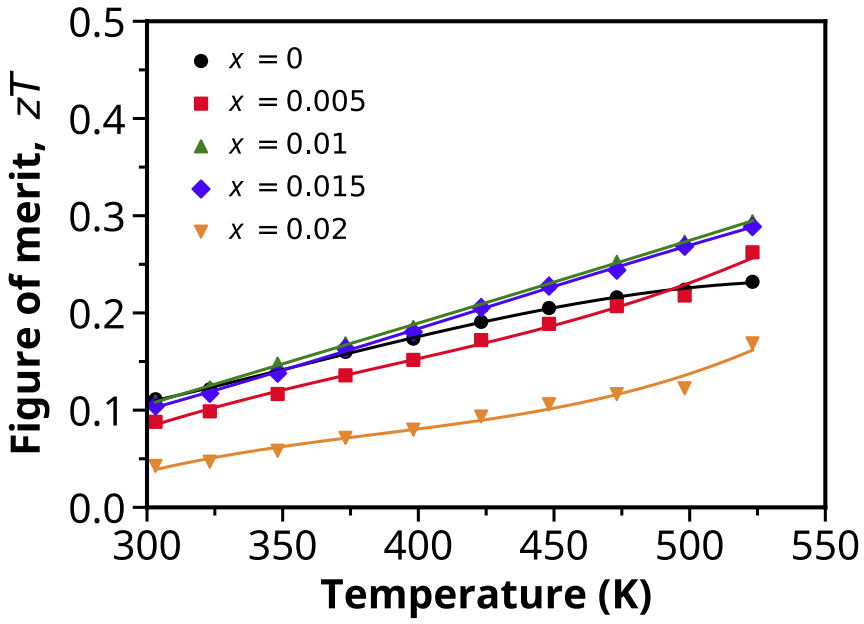

Figure 10: Figure of merit zT of $Bi_2(Te_{1.857}S_{1.142})_{1-x}I_x$ (x = 0, 0.005, 0.01, 0.015, and 0.02) between 300 to 520 K.

Conclusions

This work presents an investigation of iodine doped $Bi_{14}Te_{13}S_8$for thermoelectric applications. The intrinsic properties of $Bi_{14}Te_{13}S_8$, including its layered crystal structure, larger band gap, and intrinsically low thermal conductivity, make this compound a promising alternative to conventional Bi_2Te_3.

An optimised power factor around 3.5 $mW^2\,m^{-1}\,K^{-1}$ was achieved for a sample doped with 1 at. % iodine. Further, the lattice thermal conductivity is reduced by over 30% with iodine addition due to increased phonon scattering with the dopant presence. Samples doped with 1-1.5 at. iodine exhibit maximum zT values of ∼0.29 at 520 K, a noticeable improvement over undoped $Bi_{14}Te_{13}S_8$. This study demonstrates that iodine doping can effectively tune the

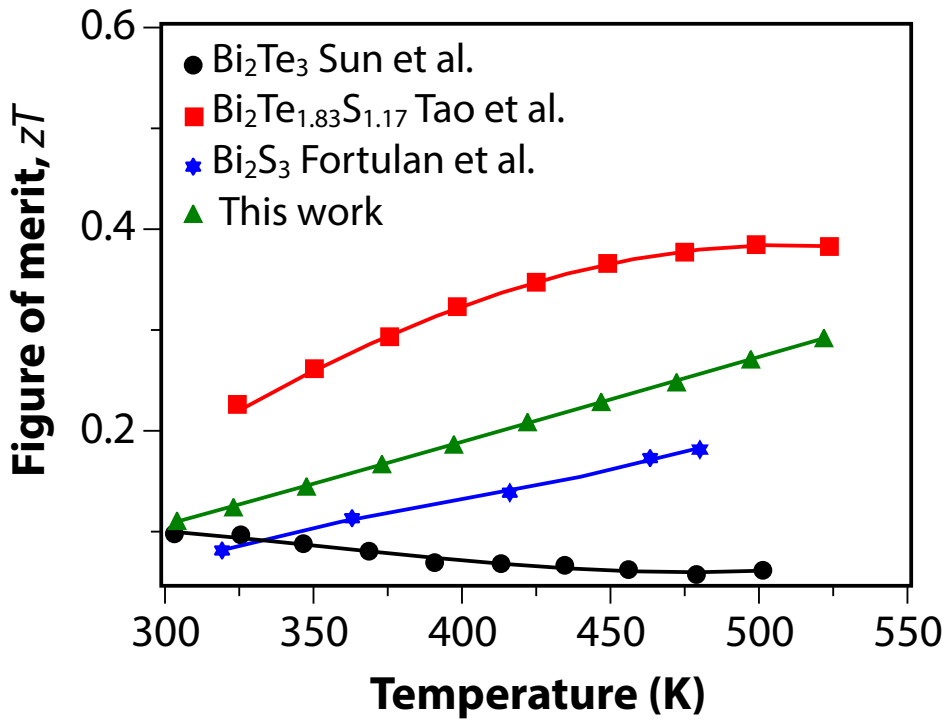

Figure 11: Comparison of the figure of merit zT values obtained in this work wit Bi_2Te_3,[5] Bi_2S_3,[29] $Bi_2Te_{1.83}S_{1.17}$,[8] and $Bi_2Te_{2.2}S_{0.8}$.[81]

electrical and thermal properties of $Bi_{14}Te_{13}S_8$ to boost its thermoelectric performance. Our results highlight the contribution of $Bi_{14}Te_{13}S_8$ to the thermoelectric properties of multiphase materials.

Acknowledgement

Acknowledgement The study has received partial funding from the European Union's Horizon 2020 research and innovation program under the Marie Skłodowska-Curie Grant Agreement No. 801604. TM would like to thank JST Mirai Program Grant Number JPMJMI19A1. IS was supported by JST SPRING, Grant Number JPMJSP2124.

References

(1) Ahmad, K.; Wan, C.; Al-Eshaikh, M. A.; Kadachi, A. N. Enhanced Thermoelectric Performance of Bi2Te3 Based Graphene Nanocomposites. *Applied Surface Science* **2019**, *474*, 2–8.

(2) Al-Alam, P.; Pernot, G.; Isaiev, M.; Lacroix, D.; De Vos, M.; Stein, N.; Osenberg, D.; Philippe, L. Lattice Thermal Conductivity of Bi2Te3 and SnSe Using Debye-Callaway and Monte Carlo Phonon Transport Modeling: Application to Nanofilms and Nanowires. *Physical Review B* **2019**, *100*, 115304.

(3) Jaworski, C. M.; Kulbachinskii, V.; Heremans, J. P. Resonant Level Formed by Tin in Bi2Te3 and the Enhancement of Room-Temperature Thermoelectric Power. *Physical Review B* **2009**, *80*, 233201.

(4) Shigetomi, S.; Mori, S. Electrical Properties of Bi2Te3. *Journal of the Physical Society of Japan* **1956**, *11*, 915–919.

(5) Sun, Y.; Qin, H.; Wang, W.; Guo, F.; Cai, W.; Sui, J. Simultaneous Regulation of Electrical and Thermal Transport Properties of N-Type Bi2Te3 via Adding Excessive Te Followed by Se Doping. *4*, 4986–4992.

(6) Tang, C.; Huang, Z.; Pei, J.; Zhang, B.-P.; Shang, P.-P.; Shan, Z.; Zhang, Z.; Gu, H.; Wen, K. Bi2Te3 Single Crystals with High Room-Temperature Thermoelectric Performance Enhanced by Manipulating Point Defects Based on First-Principles Calculation. *RSC Advances* **2019**, *9*, 14422–14431.

(7) Aminorroaya Yamini, S.; Santos, R.; Fortulan, R.; Gazder, A. A.; Malhotra, A.; Vashaee, D.; Serhiienko, I.; Mori, T. Room-Temperature Thermoelectric Performance of n-Type Multiphase Pseudobinary Bi2Te3–Bi2S3 Compounds: Synergic Effects of Phonon Scattering and Energy Filtering. *ACS Applied Materials & Interfaces* **2023**, *15*, 19220–19229.

(8) Tao, Q.; Meng, F.; Zhang, Z.; Cao, Y.; Tang, Y.; Zhao, J.; Su, X.; Uher, C.; Tang, X. The Origin of Ultra-Low Thermal Conductivity of the Bi2Te2S Compound and Boosting the Thermoelectric Performance via Carrier Engineering. *Materials Today Physics* **2021**, *20*, 100472.

(9) *Mineral Commodity Summaries 2022*; 2022.

(10) Grauer, D. C.; Hor, Y. S.; Williams, A. J.; Cava, R. J. Thermoelectric Properties of the Tetradymite-Type Bi2Te2S–Sb2Te2S Solid Solution. *Materials Research Bulletin* **2009**, *44*, 1926–1929.

(11) Joo, S.-J.; Ryu, B.; Son, J.-H.; Lee, J. E.; Min, B.-K.; Kim, B.-S. Highly Anisotropic Thermoelectric Transport Properties Responsible for Enhanced Thermoelectric Performance in the Hot-Deformed Tetradymite Bi2Te2S. *Journal of Alloys and Compounds* **2019**, *783*, 448–454.

(12) Liu, W.; Lukas, K. C.; McEnaney, K.; Lee, S.; Zhang, Q.; Opeil, C. P.; Chen, G.; Ren, Z. Studies on the Bi2Te3–Bi2Se3–Bi2S3 System for Mid-Temperature Thermoelectric Energy Conversion. *Energy & Environmental Science* **2013**, *6*, 552–560.

(13) Wang, B.; Niu, X.; Ouyang, Y.; Zhou, Q.; Wang, J. Ultrathin Semiconducting Bi2Te2S and Bi2Te2Se with High Electron Mobilities. *The Journal of Physical Chemistry Letters* **2018**, *9*, 487–490.

(14) Wu, X.; Wang, Z.; Jiang, R.; Tian, Y.; Liu, Y.; Shi, J.; Zhao, W.; Xiong, R. Enhanced Thermoelectric Performance of P-Type Bi2Te3-based Materials by Suppressing Bipolar Thermal Conductivity. *29*, 100904.

(15) Zhuang, H.-L.; Pei, J.; Cai, B.; Dong, J.; Hu, H.; Sun, F.-H.; Pan, Y.; Snyder, G. J.; Li, J.-F. Thermoelectric Performance Enhancement in BiSbTe Alloy by Microstructure Modulation via Cyclic Spark Plasma Sintering with Liquid Phase. *31*, 2009681.

(16) Yang, G.; Sang, L.; Yun, F. F.; Mitchell, D. R. G.; Casillas, G.; Ye, N.; See, K.; Pei, J.; Wang, X.; Li, J.-F.; Snyder, G. J.; Wang, X. Significant Enhancement of Thermoelectric Figure of Merit in BiSbTe-Based Composites by Incorporating Carbon Microfiber. *31*, 2008851.

(17) Pathak, R.; Dutta, P.; Srivastava, A.; Rawat, D.; Gopal, R. K.; Singh, A. K.; Soni, A.; Biswas, K. Strong Anharmonicity-Induced Low Thermal Conductivity and High n-Type Mobility in the Topological Insulator Bi1.1Sb0.9Te2S. *61*, e202210783.

(18) Hsieh, D.; Xia, Y.; Qian, D.; Wray, L.; Meier, F.; Dil, J. H.; Osterwalder, J.; Patthey, L.; Fedorov, A. V.; Lin, H.; Bansil, A.; Grauer, D.; Hor, Y. S.; Cava, R. J.; Hasan, M. Z. Observation of Time-Reversal-Protected Single-Dirac-Cone Topological-Insulator States in Bi2Te3 and SbTe3. *Physical Review Letters* **2009**, *103*, 146401.

(19) Muzaffar, M. U.; Zhu, B.; Yang, Q.; Zhou, Y.; Zhang, S.; Zhang, Z.; He, J. Suppressing Bipolar Effect to Broadening the Optimum Range of Thermoelectric Performance for P-Type Bismuth Telluride–Based Alloys via Calcium Doping. *9*, 100130.

(20) Hao, F.; Qiu, P.; Tang, Y.; Bai, S.; Xing, T.; Chu, H.-S.; Zhang, Q.; Lu, P.; Zhang, T.; Ren, D.; Chen, J.; Shi, X.; Chen, L. High Efficiency Bi 2 Te 3 -Based Materials and Devices for Thermoelectric Power Generation between 100 and 300 °C. *Energy & Environmental Science* **2016**, *9*, 3120–3127.

(21) Zhang, Z.; Cao, Y.; Tao, Q.; Yan, Y.; Su, X.; Tang, X. Distinct Role of Sn and Ge Doping on Thermoelectric Properties in P-Type (Bi, Sb)2Te3-alloys. *Journal of Solid State Chemistry* **2020**, *292*, 121722.

(22) Li, F.; Zhai, R.; Wu, Y.; Xu, Z.; Zhao, X.; Zhu, T. Enhanced Thermoelectric Performance of N-Type Bismuth-Telluride-Based Alloys via In Alloying and Hot Deformation for Mid-Temperature Power Generation. *Journal of Materiomics* **2018**, *4*, 208–214.

(23) Xu, Z.; Wu, H.; Zhu, T.; Fu, C.; Liu, X.; Hu, L.; He, J.; He, J.; Zhao, X. Attaining High Mid-Temperature Performance in (Bi, Sb) 2Te3 Thermoelectric Materials via Synergistic Optimization. *NPG Asia Materials* **2016**, *8*, e302–e302.

(24) Zhai, R.; Wu, Y.; Zhu, T.-J.; Zhao, X.-B. Tunable Optimum Temperature Range of High-Performance Zone Melted Bismuth-Telluride-Based Solid Solutions. *Crystal Growth & Design* **2018**, *18*, 4646–4652.

(25) Zhu, B.; Liu, X.; Wang, Q.; Qiu, Y.; Shu, Z.; Guo, Z.; Tong, Y.; Cui, J.; Gu, M.; He, J. Realizing Record High Performance in N-Type Bi2Te3-based Thermoelectric Materials. *13*, 2106–2114.

(26) Huang, W.; Tan, X.; Cai, J.; Zhuang, S.; Zhou, C.; Wu, J.; Liu, G.; Liang, B.; Jiang, J. Synergistic Effects Improve Thermoelectric Properties of Zone-Melted n-Type Bi2Te2.7Se0.3. *32*, 101022.

(27) Lee, H.; Kim, T.; Son, S. C.; Kim, J.; Kim, D.; Lee, J.; Chung, I. Unique Microstructures and High Thermoelectric Performance in n–Type Bi2Te2.7Se0.3 by the Dual Incorporation of Cu and Y. *31*, 100986.

(28) Wang, S.; Tan, G.; Xie, W.; Zheng, G.; Li, H.; Yang, J.; Tang, X. Enhanced Thermoelectric Properties of Bi2(Te1-xSex)3-Based Compounds as n-Type Legs for Low-Temperature Power Generation. *Journal of Materials Chemistry* **2012**, *22*, 20943–20951.

(29) Fortulan, R.; Aminorroaya Yamini, S.; Nwanebu, C.; Li, S.; Baba, T.; Reece, M. J.; Mori, T. Thermoelectric Performance of N-Type Magnetic Element Doped Bi2S3. *ACS Applied Energy Materials* **2022**,

(30) Ge, Z. H.; Zhang, B. P.; Shang, P. P.; Li, J. F. Control of Anisotropic Electrical Transport Property of Bi2S3 Thermoelectric Polycrystals. *Journal of Materials Chemistry* **2011**, *21*, 9194–9200.

(31) Ji, H.; Allred, J. M.; Fuccillo, M. K.; Charles, M. E.; Neupane, M.; Wray, L. A.; Hasan, M. Z.; Cava, R. J. Bi2Te1.6S1.4: A Topological Insulator in the Tetradymite Family. *85*, 201103.

(32) Toby, B. H.; Von Dreele, R. B. GSAS-II: The Genesis of a Modern Open-Source All Purpose Crystallography Software Package. *Journal of Applied Crystallography* **2013**, *46*, 544–549.

(33) E37 Committee *Test Method for Determining Specific Heat Capacity by Differential Scanning Calorimetry*.

(34) Perdew, J. P.; Burke, K.; Ernzerhof, M. Generalized Gradient Approximation Made Simple. *Physical Review Letters* **1996**, *77*, 3865–3868.

(35) Monkhorst, H. J.; Pack, J. D. Special Points for Brillouin-zone Integrations. *Physical Review B* **1976**, *13*, 5188–5192.

(36) Shannon, R. D. Revised Effective Ionic Radii and Systematic Studies of Interatomic Distances in Halides and Chalcogenides. *Acta crystallographica section A: crystal physics, diffraction, theoretical and general crystallography* **1976**, *32*, 751–767.

(37) Kim, J. H.; Back, S. Y.; Yun, J. H.; Lee, H. S.; Rhyee, J.-S. Scattering Mechanisms and Suppression of Bipolar Diffusion Effect in Bi2Te2.85Se0.15Ix Compounds. *Materials* **2021**, *14*, 1564.

(38) Wu, F.; Wang, W.; Hu, X.; Tang, M. Thermoelectric Properties of I-doped n-Type Bi2Te3 -Based Material Prepared by Hydrothermal and Subsequent Hot Pressing. *Progress in Natural Science: Materials International* **2017**, *27*, 203–207.

(39) Pauling, L. The Formula, Structure, and Chemical Bonding of Tetradymite, Bi14Te13S8, and the Phase Bi14Te15S6. *American Mineralogist* **1975**, *60*, 994–997.

(40) Tamtögl, A.; Campi, D.; Bremholm, M.; Hedegaard, E. M. J.; Iversen, B. B.; Bianchi, M.; Hofmann, P.; Marzari, N.; Benedek, G.; Ellis, J.; Allison, W. Nanoscale Surface Dynamics of Bi2Te3(111): Observation of a Prominent Surface Acoustic Wave and the Role of van Der Waals Interactions. *Nanoscale* **2018**, *10*, 14627–14636.

(41) Zhang, Z.; Sharma, P. A.; Lavernia, E. J.; Yang, N. Thermoelectric and Transport Properties of Nanostructured Bi $_2$ Te $_3$ by Spark Plasma Sintering. *Journal of Materials Research* **2011**, *26*, 475–484.

(42) Zhang, Z.; Sun, M.; Liu, J.; Cao, L.; Su, M.; Liao, Q.; Deng, Y.; Qin, L. Ultra-Fast Fabrication of Bi2Te3 Based Thermoelectric Materials by Flash-Sintering at Room Temperature Combining with Spark Plasma Sintering. *Scientific Reports* **2022**, *12*, 10045.

(43) Nagao, J.; Ferhat, M.; Hatta, E.; Mukasa, K. Anisotropic Factor of Electrical Conductivity in P-Bi2Te3 Crystals. *physica status solidi (b)* **2000**, *219*, 347–349.

(44) Byrnes, J. B.; Gazder, A. A.; Yamini, S. A. Assessing Phase Discrimination via the Segmentation of an Elemental Energy Dispersive X-ray Spectroscopy Map: A Case Study of Bi2Te3 and Bi2Te2S. *RSC Advances* **2018**, *8*, 7457–7464.

(45) Cava, R. J.; Ji, H.; Fuccillo, M. K.; Gibson, Q. D.; Hor, Y. S. Crystal Structure and Chemistry of Topological Insulators. *Journal of Materials Chemistry C* **2013**, *1*, 3176–3189.

(46) Crowley, J. M.; Tahir-Kheli, J.; Goddard, W. A. Resolution of the Band Gap Prediction Problem for Materials Design. *The Journal of Physical Chemistry Letters* **2016**, *7*, 1198–1203.

(47) Mori-Sánchez, P.; Cohen, A. J.; Yang, W. Localization and Delocalization Errors in Density Functional Theory and Implications for Band-Gap Prediction. *Physical Review Letters* **2008**, *100*, 146401.

(48) Perdew, J. P.; Levy, M. Physical Content of the Exact Kohn-Sham Orbital Energies: Band Gaps and Derivative Discontinuities. *Physical Review Letters* **1983**, *51*, 1884–1887.

(49) Perdew, J. P.; Zunger, A. Self-Interaction Correction to Density-Functional Approximations for Many-Electron Systems. *Physical Review B* **1981**, *23*, 5048–5079.

(50) Sham, L. J.; Schlüter, M. Density-Functional Theory of the Energy Gap. *Physical Review Letters* **1983**, *51*, 1888–1891.

(51) Pribram-Jones, A.; Gross, D. A.; Burke, K. DFT: A Theory Full of Holes? *Annual Review of Physical Chemistry* **2015**, *66*, 283–304.

(52) Fiolhais, C.; Nogueira, F.; Marques, M. A. L. *A Primer in Density Functional Theory*; Springer Science & Business Media, 2003.

(53) Sham, L. J.; Kohn, W. One-Particle Properties of an Inhomogeneous Interacting Electron Gas. *Physical Review* **1966**, *145*, 561–567.

(54) Saal, J. E., Kirklin, S., Aykol, M., Meredig, B., and Wolverton, C. Bi14Te13S8. https://oqmd.org/materials/entry/101967.

(55) National Institute of Standards and Technology (NIST) JVASP-29442_Bi14Te13S8. https://www.ctcms.nist.gov/~knc6/jsmol/JVASP-29442.html.

(56) Mp-557619: Bi14Te13S8 (Trigonal, R-3, 148). https://next-gen.materialsproject.org/materials/mp-557619/.

(57) Rashid, Z.; Nissimagoudar, A. S.; Li, W. Phonon Transport and Thermoelectric Properties of Semiconducting Bi $_2$ Te $_2$ X (X = S, Se, Te) Monolayers. *Physical Chemistry Chemical Physics* **2019**, *21*, 5679–5688.

(58) Su, D.; Cheng, J.; Li, S.; Zhang, S.; Lyu, T.; Zhang, C.; Li, J.; Liu, F.; Hu, L. Inhibiting the Bipolar Effect via Band Gap Engineering to Improve the Thermoelectric Performance in N-Type Bi2-xSbxTe3 for Solid-State Refrigeration. *138*, 50–58.

(59) Chen, L.; Zhang, Q.; Guo, Z.; Yan, Z.; Song, K.; Wu, G.; Wang, X.; Tan, X.; Hu, H.; Sun, P.; Liu, G.-Q.; Jiang, J. Expand Band Gap and Suppress Bipolar Excitation to Optimize Thermoelectric Performance of Bi0.35Sb1.65Te3 Sintered Materials. *21*, 100544.

(60) Zhang, L.; Xiao, P.; Shi, L.; Henkelman, G.; Goodenough, J. B.; Zhou, J. Suppressing the Bipolar Contribution to the Thermoelectric Properties of Mg2Si0.4Sn0.6 by Ge Substitution. *117*, 155103.

(61) Xiao, Y.; Wu, H.; Cui, J.; Wang, D.; Fu, L.; Zhang, Y.; Chen, Y.; He, J.; Pennycook, S. J.; Zhao, L.-D. Realizing High Performance N-Type PbTe by Synergistically Optimizing Effective Mass and Carrier Mobility and Suppressing Bipolar Thermal Conductivity. *11*, 2486–2495.

(62) Wang, S.; Yang, J.; Toll, T.; Yang, J.; Zhang, W.; Tang, X. Conductivity-Limiting Bipolar Thermal Conductivity in Semiconductors. *5*, 10136.

(63) Jonson, M.; Mahan, G. D. Mott's Formula for the Thermopower and the Wiedemann-Franz Law. *Physical Review B* **1980**, *21*, 4223–4229.

(64) Goldsmid, H. J. Bismuth Telluride and Its Alloys as Materials for Thermoelectric Generation. *Materials (Basel)* **2014**, *7*, 2577–2592.

(65) Goldsmid, H. J. The Electrical Conductivity and Thermoelectric Power of Bismuth Telluride. *Proceedings of the Physical Society* **1958**, *71*, 633–646.

(66) Han, M.-K.; Yu, B.-G.; Jin, Y.; Kim, S.-J. A Synergistic Effect of Metal Iodide Doping

on the Thermoelectric Properties of Bi2Te3. *Inorganic Chemistry Frontiers* **2017**, *4*, 881–888.

(67) Yang, J.; Liu, G.; Yan, J.; Zhang, X.; Shi, Z.; Qiao, G. Enhanced the Thermoelectric Properties of N-Type Bi2S3 Polycrystalline by Iodine Doping. *728*, 351–356.

(68) Witting, I. T.; Chasapis, T. C.; Ricci, F.; Peters, M.; Heinz, N. A.; Hautier, G.; Snyder, G. J. The Thermoelectric Properties of Bismuth Telluride. *Advanced Electronic Materials* **2019**, *5*.

(69) Witting, I. T.; Ricci, F.; Chasapis, T. C.; Hautier, G.; Snyder, G. J. The Thermoelectric Properties of n -Type Bismuth Telluride: Bismuth Selenide Alloys Bi2Te3-xSex. *Research* **2020**, *2020*, 1–15.

(70) Pei, J.; Zhang, L.-J.; Zhang, B.-P.; Shang, P.-P.; Liu, Y.-C. Enhancing the Thermoelectric Performance of CexBi2S3 by Optimizing the Carrier Concentration Combined with Band Engineering. *Journal of Materials Chemistry C* **2017**, *5*, 12492–12499.

(71) Chen, B.; Uher, C.; Iordanidis, L.; Kanatzidis, M. G. Transport Properties of Bi2S3 and the Ternary Bismuth Sulfides KBi6.33S10 and K2Bi8S13. *Chemistry of Materials* **1997**, *9*, 1655–1658.

(72) Landau, L. D.; Lifshitz, E. M. *Statistical Physics: Volume 5*; Elsevier, 2013.

(73) Attard, P. *Thermodynamics and Statistical Mechanics: Equilibrium by Entropy Maximisation*; Academic Press, 2002.

(74) Dongre, B.; Carrete, J.; Wen, S.; Ma, J.; Li, W.; Mingo, N.; Madsen, G. K. H. Combined Treatment of Phonon Scattering by Electrons and Point Defects Explains the Thermal Conductivity Reduction in Highly-Doped Si. *Journal of Materials Chemistry A* **2020**, *8*, 1273–1278.

(75) Fava, M.; Protik, N. H.; Li, C.; Ravichandran, N. K.; Carrete, J.; van Roekeghem, A.; Madsen, G. K. H.; Mingo, N.; Broido, D. How Dopants Limit the Ultrahigh Thermal Conductivity of Boron Arsenide: A First Principles Study. *npj Computational Materials* **2021**, *7*, 1–7.

(76) Pei, Y.-L.; He, J.; Li, J.-F.; Li, F.; Liu, Q.; Pan, W.; Barreteau, C.; Berardan, D.; Dragoe, N.; Zhao, L.-D. High Thermoelectric Performance of Oxyselenides: Intrinsically Low Thermal Conductivity of Ca-doped BiCuSeO. *NPG Asia Materials* **2013**, *5*, e47–e47.

(77) Zapata-Arteaga, O.; Perevedentsev, A.; Marina, S.; Martin, J.; Reparaz, J. S.; Campoy-Quiles, M. Reduction of the Lattice Thermal Conductivity of Polymer Semiconductors by Molecular Doping. *ACS Energy Letters* **2020**, *5*, 2972–2978.

(78) Zhang, P.; Liao, W.; Zhu, Z.; Qin, M.; Zhang, Z.; Jin, D.; Liu, Y.; Wang, Z.; Lu, Z.; Xiong, R. Tuning the Lattice Thermal Conductivity of Sb2Te3 by Cr Doping: A Deep Potential Molecular Dynamics Study. *Physical Chemistry Chemical Physics* **2023**, *25*, 15422–15432.

(79) Wang, H.; Chen, J.; Lu, T.; Zhu, K.; Li, S.; Liu, J.; Zhao, H. Enhanced Thermoelectric Performance in P-Type Mg $_{3}$ Sb $_{2}$ via Lithium Doping. *27*, 047212.

(80) Freer, R. et al. Key Properties of Inorganic Thermoelectric Materials—Tables (Version 1). *Journal of Physics: Energy* **2022**, *4*, 022002.

(81) Malik, I.; Srivastava, T.; Surthi, K. K.; Gayner, C.; Kar, K. K. Enhanced Thermoelectric Performance of N-Type Bi2Te3 Alloyed with Low Cost and Highly Abundant Sulfur. *255*, 123598.